Structural and magnetic properties of $CuCl_2$ graphite intercalation compounds

Masatsugu Suzuki, Itsuko S. Suzuki, and Charles R. Burr
Department of Physics, State University of New York at Binghamton, Binghamton, New York 13902-6000

David G. Wiesler and Nicholas Rosov
National Institute of Standards and Technology, Gaithersburg, Maryland 20899

Kei-ichi Koga
Institute for Solid State Physics, University of Tokyo, Minato-ku, Tokyo 106, Japan
(Received 20 May 1994)

Structural and magnetic properties of stage-1, stage-2, and stage-3 $CuCl_2$ graphite intercalation compounds (GIC's) were studied by means of x-ray, electron- and neutron-diffraction, dc magnetic susceptibility, and electron spin resonance (ESR) measurements. The Cu^{2+} ions form an isosceles triangular lattice with one short side and two longer sides. The in-plane dc magnetic susceptibility shows Curie-Weiss behavior above 150 K, a broad maximum around 62–65 K, indicative of low-dimensional magnetic correlations, and a Curie-type behavior below 20 K, attributable to paramagnetic inhomogeneities in the sample. The temperature and magnitude of the susceptibility maximum are more consistent with a two-dimensional Heisenberg antiferromagnet than a one-dimensional model, suggesting that the distortion from an equilateral triangular lattice is not an important factor in the magnetic behavior of $CuCl_2$ GIC's. ESR measurements indicate that the local magnetic symmetry of Cu^{2+} spins is tetragonal. The angular dependence of the ESR linewidth at 4.2 K is explained by the combined effects of a canting of the tetragonal axis from the c axis and a weak anisotropy in the Landé g factor that favors spins to lie in the intercalate plane. No magnetic phase transition is observed from dc magnetic susceptibility down to 1.5 K and magnetic neutron scattering above 0.5 K.

I. INTRODUCTION

It has been theoretically accepted that spin frustration plays an important role in antiferromagnets on the triangular lattice (AFT).[1–4] The phase transition of the classical AFT model depends on the nature of the spin asymmetry: Ising, XY, or Heisenberg. When interactions are restricted to nearest-neighbor spins, the AFT Ising model shows no phase transition at any temperature because of a degeneracy of the ground state caused by spin frustration.[1] In the case of AFT XY model, the ground state consists of spins on three sublattices at 120° angles with respect to each other. Because the ground state has a twofold degeneracy due to helicity, as well as an XY-like continuous degeneracy, it undergoes two phase transitions, one associated with the Ising-type symmetry-breaking mechanism and other with a Kosterlitz-Thouless mechanism.[2,3] For Heisenberg symmetry, the AFT model predicts a more complex phase transition, driven by the dissociation of pairs of vortices formed of chirality vectors.[4]

An established way to test these theories is through the use of two-dimensional (2D) magnetic prototypes. In this context magnetic graphite intercalation compounds (GIC's) have received considerable attention.[5,6] The effective dimensionality of magnetic GIC's can be decreased by increasing the stage number, the number of graphite layers between magnetic intercalate layers.

Magnetic measurements on $CuCl_2$ GIC's and $MnCl_2$ GIC's suggest that the AFT model may be realized in these two systems. $MnCl_2$ GIC approximates a 2D XY antiferromagnet on an equilateral triangular lattice.[7–10] For $CuCl_2$ GIC the lattice is distorted into an isosceles triangular lattice with one short side and two longer sides.[11–14] The spin symmetry is expected to be Heisenberg-like with $S=\frac{1}{2}$. Because of the lattice distortion, the exchange interaction between nearest-neighbor Cu^{2+} spins along the short axis (J_1) may be different from that along the longer axis (J_2). If $|J_1|\approx|J_2|$ then $CuCl_2$ GIC's may provide a model system for studying the phase transition of the 2D AFT Heisenberg model. Conversely, if $|J_1|\gg|J_2|$ then $CuCl_2$ GIC's may behave like a one-dimensional (1D) antiferromagnet along the short axis.

In spite of this special interest, $CuCl_2$ GIC's have not been thoroughly investigated. The in-plane structure and stacking sequence of $CuCl_2$ GIC have been studied by Hauw *et al.*[15] and Speck *et al.*[16] with x-ray diffraction and electron microscopy, and by Wiesler[14] with neutron diffraction. The magnetic properties have been studied by Nishihara *et al.*[11] and Rancourt, Meschi, and Flandrois[13] with dc magnetic susceptibility, and by Koga, Suzuki, and Yasuoka[12] with electron spin resonance (ESR). The dc susceptibility exhibits a broad maximum between 65 and 70 K. There is some suggestion, too, of a dc susceptibility anomaly around 14 K, reported for stage-1 $CuCl_2$ GIC by Nishihara *et al.*[11] and for stage-2 $CuCl_2$ GIC by Rancourt, Meschi, and Flandrois.[13] However, no definitive evidence has been forthcoming for the existence of either a phase transition or a magnetically

ordered phase.

In this paper, we report experimental results on the structural and magnetic properties of stage-1, stage-2, and stage-3 $CuCl_2$ GIC's. We present measurements of the in-plane structure and stacking sequence by x-ray, electron, and neutron diffraction, and the magnetic properties by dc magnetic susceptibility, electron spin resonance (ESR), and magnetic neutron scattering. The temperature dependence of the dc magnetic susceptibility is compared to predictions for 2D and 1D Heisenberg antiferromagnets and is most consistent with the 2D model, contrary to other claims.[13] No evidence for a magnetic phase transition is observed by either dc susceptibility measurements above 1.5 K or magnetic neutron scattering above 0.5 K. The angular dependence of the g factor and the ESR linewidth is explained in terms of a local tetragonal symmetry of Cu^{2+} ions.

II. BACKGROUND

A. Crystal structure of $CuCl_2$ GIC

Pristine $CuCl_2$ has a monoclinic crystal structure with space group $C2/m$, whose lattice parameters are given by $a'=6.85$ Å, $b'=3.30$ Å, $c'=6.70$ Å, $\alpha'=\gamma'=90°$, and

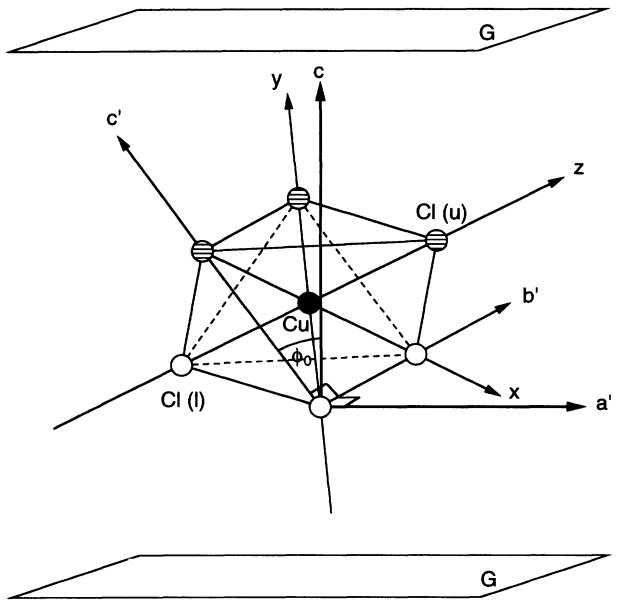

(a)

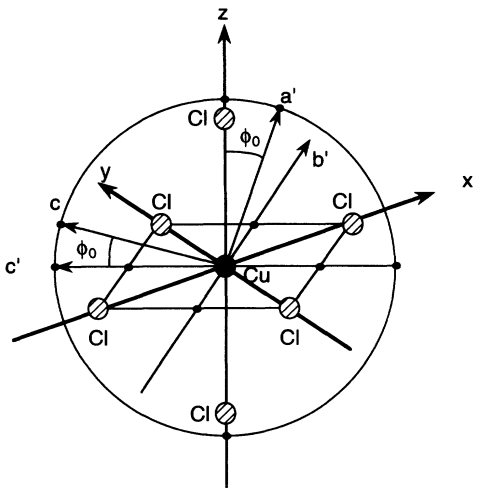

(b)

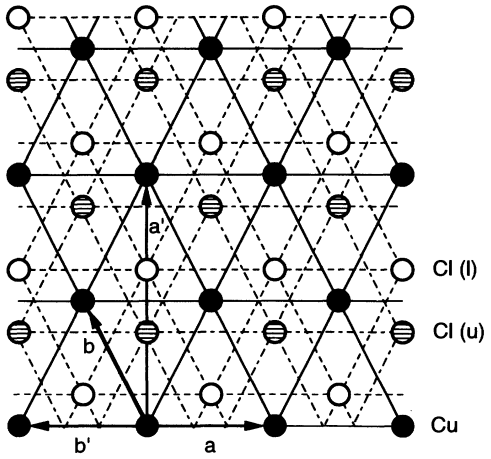

(c)

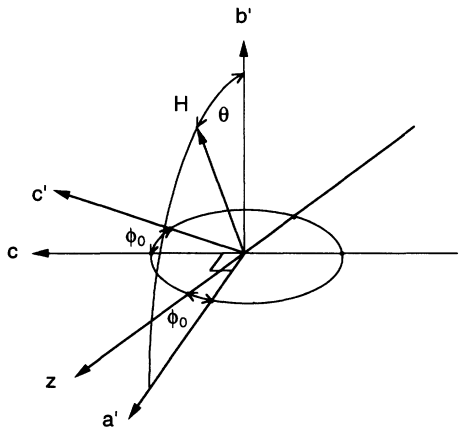

(d)

FIG. 1. (a) Schematic crystal structure of $CuCl_2$ GIC's. The a', b', and c axes are orthogonal. (b) Unit octahedron consisting of one Cu^{2+} ion and six Cl^- ions. The z axis is the local tetragonal axis, and the a', z, c, and c' axes lie in the same plane. The x and y axes give the directions from a Cu^{2+} ion to its nearest-neighbor Cl^- ions in the b'-c' plane. (c) In-plane structure of the $CuCl_2$ intercalate layers. The Cu layer is sandwiched between the upper (shaded circles) and lower (open circles) Cl layers. **a** and **b** are the primitive lattice vectors of the $CuCl_2$ layer where $\mathbf{a}'=2\mathbf{b}+\mathbf{a}$ and $\mathbf{b}'=-\mathbf{a}$. (d) Coordinate system for stage-2 $CuCl_2$ GIC. The magnetic field **H** lies in the a'-b' plane for ESR measurements.

$\beta' = 121°$.[17] In the a'-b' plane, where the closest packing of Cu^{2+} ions occurs, the Cu^{2+} ions form an isosceles triangular lattice, defined by $\mathbf{a} = -\mathbf{b}'$ and $\mathbf{b} = (\mathbf{a}' + \mathbf{b}')/2$ and consisting of one short leg ($a = 3.30$ Å) and two longer legs ($b = 3.80$ Å), with an angle between them of 115.74°. Intercalation into graphite nearly preserves the structure of the a'-b' (or a-b) plane.[14–16]

Figure 1(a) shows the schematic crystal structure of $CuCl_2$ GIC. The a'-b' plane coincides with the hexagonal plane of graphite (with lattice constants $|\mathbf{a}_G| = |\mathbf{b}_G| = 2.46$ Å). Within each intercalate layer, a Cu plane is sandwiched between upper and lower Cl layers. As shown in Fig. 1(b), each Cu^{2+} ion is located at the center of a deformed octahedron consisting of six Cl^- ions. A tetragonal deformation results in four shorter Cu-Cl distances (2.39 Å) in the b'-c' plane and two longer ones (2.95 Å) perpendicular to this plane, along the local tetragonal axis (z axis). This axis and the GIC c axis lie in the c'-a' plane, as shown in Fig. 1(b), such that the angle ϕ_0 between the c axis and c' axis is 31°. The x and y axes give the directions from a Cu^{2+} ion to its nearest-neighbor Cl^- ions in the b'-c' plane [see Fig. 1(b)]. Figure 1(c) shows the in-plane structure of the $CuCl_2$ intercalate layer.

B. Magnetic properties of pristine $CuCl_2$

The magnetic properties of pristine $CuCl_2$ (with spin $S = \frac{1}{2}$) have been studied by heat-capacity and magnetization measurements,[18–23] which show a transition to antiferromagnetic order at $T_N = 23.9$ K. The heat capacity shows a sharp peak at T_N and a broad peak at $T(C_{max}) = 40$ K.[19] The dc magnetic susceptibility shows a broad peak at $T(\chi_{max}) = 70$ K and obeys a Curie-Weiss law at high temperatures with a Curie-Weiss temperature $\Theta = -109$ K.[18] De Jongh and Miedema[24] have shown that due to the relatively high value of $T_N \sim 0.6T(C_{max})$ and the large amount of entropy gained below T_N (17% of R ln2, where $R = 1.9862$ cal/mol K), pristine $CuCl_2$ is a poor example of a linear chain antiferromagnet.

The Cu^{2+} ions in pristine $CuCl_2$ have fourfold symmetry in the b'-c' planes. Billerey *et al.* have explained the dc magnetic susceptibility[20,21] and heat capacity[23] by assuming that $CuCl_2$ behaves like a 2D planar Heisenberg antiferromagnet with four nearest-neighbor Cu^{2+} ions ($z = 4$) and a nearest-neighbor exchange interaction J of -37 K. The field-dependent magnetization along the b' axis at 4.2 K undergoes a spin flop at 40.6 kOe.[21,22] The spin-flop field H_{SF} at 0 K is described by $H_{SF} = (2H_E H_A)^{1/2}$, where H_E is the exchange field defined as $H_E = (2z|J|S/g\mu_B)$, H_A is the anisotropy field, and g is the Landé g factor. For $g \approx 2$, H_E is estimated to be 2×10^6 Oe, and $H_A = 400$ Oe from the relation above. The extremely small ratio of H_A/H_E (on the order of 10^{-4}) indicates that the spin symmetry of the pristine compound is almost isotropic, and that $CuCl_2$ behaves like a Heisenberg antiferromagnet.

III. EXPERIMENT

The $CuCl_2$ GIC samples were prepared by heating a mixture of anhydrous $CuCl_2$ powder and single crystals of kish graphite in vacuum-sealed Pyrex glass tubing at 510 °C for stage-1 samples or 440 °C for stage-2 and stage-3 samples. The reactions were continued for 14 days. The stoichiometry of these compounds was determined from weight uptake (Table I). The c-axis repeat distance d of samples used for susceptibility and ESR measurements was determined at 293 K from ($00L$) x-ray diffraction, using a Huber double-circle diffractometer with a Siemens 2.0-kW x-ray generator, and is listed in Table I. The uncertainty in d for sample no. 4 is large because of Hendricks-Teller-type stage disorder along the c axis.[25,26]

The dc magnetic susceptibility was measured by a Faraday balance. Data were collected for temperatures between 1.5 and 300 K using a 4-kOe magnetic field applied in an arbitrary direction in the a-b plane. The ESR experiment was performed by conventional audio frequency field-modulated spectrometers at the microwave frequency of $\nu = 22.8$ GHz. The sample was set in the fixed frequency TE_{101} mode cavity, and the g value and linewidth were measured between 1.38 and 300 K with the magnetic field applied in the a-b plane. Electron diffraction was carried out at 100 K using a Hitachi HU 500 electron microscope operated at 350 kV and located at the Institute for Solid State Physics of the University of Tokyo (Japan).

Elastic neutron-scattering experiments were performed on triple-axis spectrometers using several different cryostats. Preliminary measurements were made down to 9 K at the HFIR at Oak Ridge National Laboratory. Spectrometers at the National Institute of Standards and Technology (NIST) were used for more detailed measurements and to extend the temperature range down to 0.5 K. Table II shows the experimental configuration and approximate longitudinal resolution (at 2 $Å^{-1}$) for each spectrometer. In all cases the monochromator and analyzer were graphite(002), and a filter was used to eliminate $\lambda/2$ contamination.[27]

The neutron-scattering samples were predominantly stage 1. That used in the HFIR experiments was based on a large piece of kish graphite, about 300 mg after intercalation. For measurements at NIST additional pieces of HOPG-based $CuCl_2$ GIC were added to this, producing a sample of 1.3 gm with a c-axis mosaic spread of 10° and isotropic in-plane mosaicity. The samples were

TABLE I. Characterization of samples having stoichiometry of C_nCuCl_2.

Sample number	n	Stage number	d spacing (Å)
1	4.80	1	9.44±0.01
2	4.50	1	9.44±0.01
3	9.65	2	12.81±0.05
4	12.10	3	16.32±0.35
5 (neutron)		1	9.43±0.01

TABLE II. Spectrometer configurations for triple-axis neutron measurements. The resolution is calculated below for $Q=2.0$ Å^{-1}.

Lab.	Spectrometer	Energy (meV)	λ (A°)	Collimation (min)	Resolution (Å^{-1})	Filter	Cryostat
ORNL	HB2	14.8	2.351	60-40-40-60	0.024	Graphite	Closed-cycle ^{4}He
NIST	BT9	14.8	2.351	40-48-48-200	0.024	Graphite	None
NIST	BT2	13.7	2.443	60-40-40-80	0.024	Graphite	^{3}He
NIST	SPINS	4.62	4.208	50-40-80-200	0.012	Be	^{3}He

oriented so that the scattering plane was defined by the c axis and a powder averaged a-b axis. Since the intercalate sublattice is incommensurate with the graphite sublattice, reflections can be indexed relative to either by preceding the Miller indices with a "Cu" or "G." Intercalate indices will be referred to the isosceles lattice. To distinguish stage-1 reflections from the weaker stage-2 reflections, we shall subscript $(00L)$ peaks with the stage number.

IV. RESULT AND DISCUSSION

A. Structure of stage-1 $CuCl_2$ GIC

1. c-axis structure

Figure 2 shows the neutron-scattering intensity at 30 K in the $[00L]$ direction. The most intense peaks can be indexed to stage-1 reflections, with a c-axis repeat distance of 9.35 Å (9.43 Å at 295 K). As evident from the weaker peaks, 5–10% of the sample consists of stage-2 $CuCl_2$ GIC and 1–2% unintercalated sample is also present. Al diffraction peaks from the sample are observed.

The c-axis mosaic structure is shown by rocking the sample through the $(002)_1$ peak at 1.345 Å^{-1} (Fig. 3). Near the peak center ($\omega=0$) the curve is roughly Gaussian, with a full width at half maximum (FWHM) of 10°. However, the rocking curve shows long tails, which are above background for all ω. (We take as background the intensity for a similar rocking curve at $Q=1.25$ Å^{-1}; this has been subtracted out of the data shown in Fig. 3.) One implication of this broad mosaic spread is that the intense $(00L)_1$ reflections appear as weak powder rings in scans away from the c axis.

2. In-plane structure

Figure 4 shows the in-plane electron-diffraction pattern of stage-1 $CuCl_2$ GIC (sample no. 1) at 100 K. Open circles represent the G(100) reflections at scattering vector $|\mathbf{a}_G^*|=|\mathbf{b}_G^*|=2.95$ Å^{-1}. The intercalate layer consists of three domains denoted I, II and III, where domains II and III are generated by rotating domain I by ±120° about the c axis. The spots indicated by solid circles, triangles, and squares in Fig. 4 represent the $CuCl_2$ reflections which can be indexed to the oblique cells of domains I, II and III, respectively. The principal $CuCl_2$ reflections from domain I occur at $|\mathbf{a}^*|=2.124\pm0.005$ Å^{-1} and $|\mathbf{b}^*|=1.88\pm0.005$ Å^{-1}. These positions of the diffraction spots indicate that (i) the $CuCl_2$ intercalate layer is incommensurate with the graphite layer and (ii) the a axis of the $CuCl_2$ intercalate

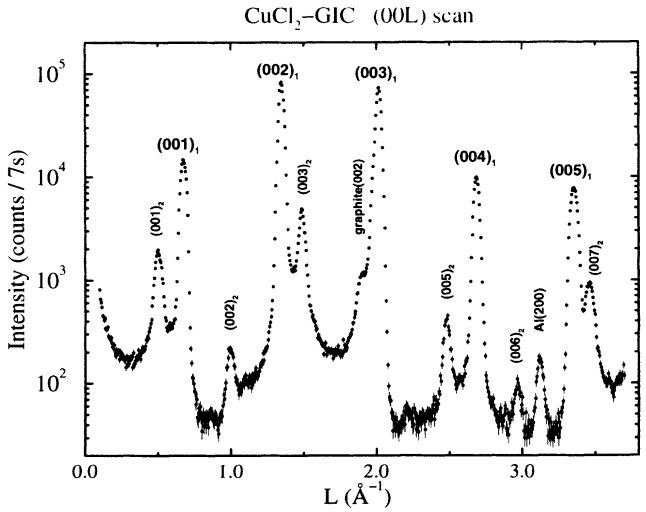

FIG. 2. Neutron-scattering intensity (taken on BT9) at about 30 K from stage-1 $CuCl_2$ GIC along (00L), perpendicular to the intercalate plane. Peaks are indexed with subscripts that give their stage number. Intensity ratios indicate 5–10% stage-2 contamination and 1–2% unintercalated graphite in the sample.

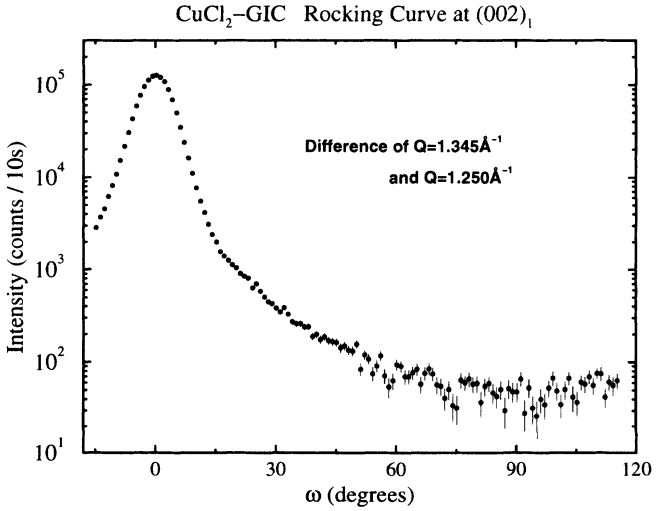

FIG. 3. Rocking curve (measured on BT2) through the stage-1 (002) reflection at $Q=1.345$ Å^{-1}. The "background" is estimated by a similar scan at $Q=1.250$ Å^{-1} and has been subtracted out in this curve. The intensity never reaches zero, indicating substantial orientational disorder in the GIC.

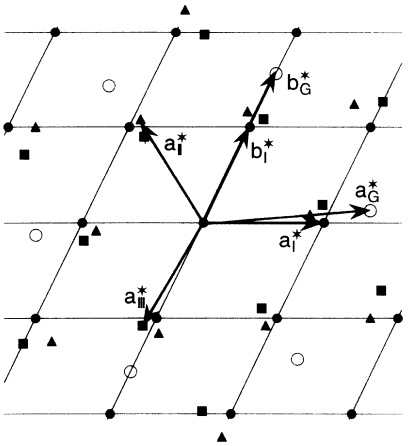

FIG. 4. In-plane electron-diffraction pattern of stage-1 $CuCl_2$ GIC measured at 100 K. The solid circles, triangles, and squares denote the Bragg reflections from domains I, II, and III of $CuCl_2$ layers, respectively, and open circles from graphite layers, where $\{\mathbf{a}_G^*,\mathbf{b}_G^*\}$ and $\{\mathbf{a}^*,\mathbf{b}^*\}$ are the sets of the primitive reciprocal-lattice vectors of graphite layers and $CuCl_2$ layers, respectively.

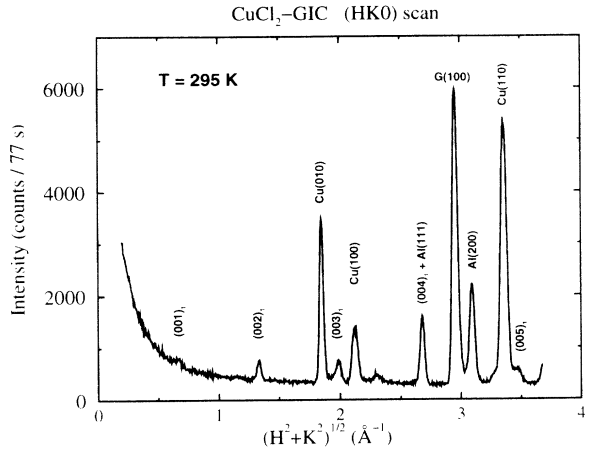

FIG. 5. Neutron-scattering intensity (measured on BT9) along (*HK*0) at room temperature. Prominent peaks are indexed to intercalate or graphite sublattices. There is a weaker contribution from the Al sample can and from the $(00L)_1$ powder rings.

layer coincides with the graphite a_G axis.

Because the neutron sample is isotropic in the **a**-**b** plane, the intensity for an in-plane neutron scan will be approximately a circular average of Fig. 4. Figure 5 shows the room-temperature neutron-scattering intensity of stage-1 $CuCl_2$ GIC along the powder-averaged (HK0) direction. Prominent peaks can be indexed to either the intercalated $CuCl_2$ or the graphite sublattices. In addition, there are Al reflections from the sample can and several $(00L)_1$ peaks present, associated with the long tails of the *c*-axis mosaic spread. In near agreement with the electron-diffraction results, the Cu(100) and Cu(010) reflections are observed at 2.125 ± 0.005 Å^{-1} and 1.850 ± 0.005 Å^{-1}, respectively. This indicates that the $CuCl_2$ layer forms an isosceles triangular lattice with lattice constants $a=3.28$ Å and $b=3.77$ Å and with an angle $\psi_0=115.8°$ between the *a* and *b* axes. These lattice parameters are nearly the same as those in pristine $CuCl_2$.

3. *Stacking structure*

Figure 6 shows the neutron-diffraction data above any possible ordering temperature along Cu(01*L*), Cu(10*L*), and G(10*L*). To understand the observed intensities, we plot all the peaks seen for these, the (*HK*0), and the (00*L*) scans in Fig. 7. The solid squares indicate intense $(00L)_1$ reflections, which, because of the *c*-axis mosaic, trace out powder rings indicated by solid circular arcs. Two Al powder rings from the sample can and cryostat heat shields are shown also as dotted arcs. According to this diagram, several of the peaks in Fig. 6 are due in part to Al or $(00L)_1$ powder rings.

Indexing *L* relative to the stage-1 *c*-axis repeat distance *d*, we find Bragg reflections at integral *L* for the Cu(01*L*) scan and half-odd-integral *L* for the G(10*L*) and Cu(10*L*) scans (see Fig. 7). The same results are reported by Speck

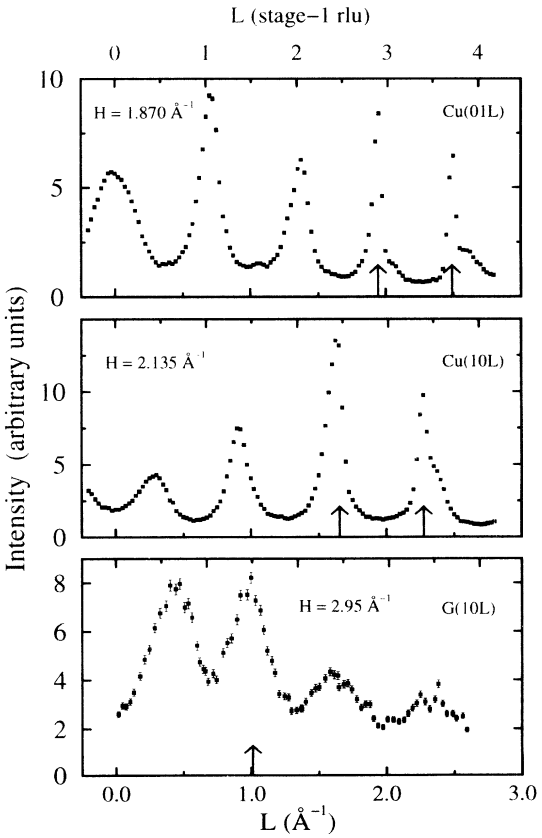

FIG. 6. Neutron-scattering intensity along Cu(01*L*) and Cu(10*L*) at 35 K and G(10L) at 9.0 K. The top two scans were performed on BT2; identical scans at 0.5 K show no additional intensity due to magnetic order. The G(10L) scan was performed at Oak Ridge on line HB2. Arrows indicate the positions of Al powder reflections from the sample can and cryostat shroud. The upper *x*-axis label refers to *L* in stage-1 reciprocal-lattice units at 35 K, $c^*=(2\pi/9.35)$ Å^{-1}.

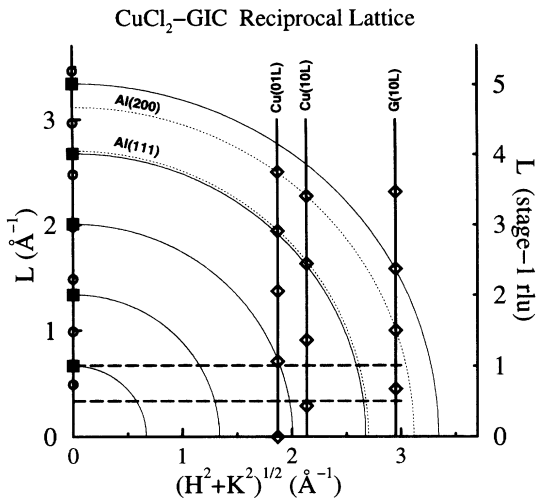

FIG. 7. Reciprocal space diagram for $CuCl_2$ GIC. The vertical axis points perpendicular to the intercalate plane, and the horizontal axis is a powder-averaged in-plane direction. The intense $(00L)_1$ peaks are shown as solid squares, which because of sample mosaicity have some intensity distributed along the solid circular arcs. $(00L)_2$ peaks are shown as open circles. Off-specular rods are shown as bold vertical lines, with the peaks from the scans in Fig. 6 shown as open diamonds. Solid and dashed bold lines show scan directions searched for magnetic scattering.

et al.[16] from x-ray precession photography and imply a doubling of the unit cell along the c axis, so that the supercell repeat distance $c_0=2d$. This doubling can be explained by a stacking sequence $A\alpha B\beta A\alpha B\beta\ldots$, where the graphite layers are indicated by Roman letters and the $CuCl_2$ layer by Greek letters. The stacking is, however, imperfect. Even though Cu(100) and G(100) are not maxima on the L scans of Fig. 6, they appear as peaks in $(HK0)$ scans in Fig. 5. This implies that Cu($10L$), Cu($01L$), and G($10L$) are modulated diffraction rods, which arise from substantial stacking disorder.

What is the detailed stacking relation between adjacent $CuCl_2$ planes? Let $\delta=\delta_1\mathbf{a}+\delta_2\mathbf{b}$ represent the in-plane translation vector between the α- and β-$CuCl_2$ layers. Similarly, let $\delta_G=(\mathbf{a}_G-\mathbf{b}_G)/3$ be the in-plane translation vector between the A- and B-graphite layers, which we take to be the same as for pristine graphite. The Cl^- positions are given relative to Cu^{2+} as $\pm\Delta=\pm\{z_{0_c}+p[(\frac{1}{2})\mathbf{a}+\mathbf{b}]\}$, where for pristine $CuCl_2$ $p=0.75$ and $z_0=1.50$ Å. The structure factor (for H and K not both equal to zero) is then

$$F_{\mathrm{Cu}(HKL)}=\left[b_{\mathrm{Cu}}+2b_{\mathrm{Cl}}\cos\left[\frac{z_0}{c_0}\pi L+\phi(HK)\right]\right]\times\left\{1+\exp\left[2\pi i\left[\frac{L}{2}+\delta_1H+\delta_2K\right]\right]\right\}, \quad (1)$$

where $\phi(HK)=\pi p(H+2K)$, b_i is the scattering length of the ith atom, and L is now indexed in units of $2\pi/c_0$. Since systematic absences occur at $L=1,3,5,\ldots$ for Cu($01L$) and at $L=0,2,4,\ldots$ for Cu($10L$), the last factor in Eq. (1) implies that $\delta_1=\frac{1}{2}$ and $\delta_2=0$; that is, $\delta=\mathbf{a}/2$. Atomic configurations with $\pm p$ should be equally probable. Therefore, the unit-cell scattering function can be written

$$S_{\mathrm{Cu}(HKL)}=\left\{\left[b_{\mathrm{Cu}}+2b_{\mathrm{Cl}}\cos\left[\frac{z_0}{c_0}\pi L+\phi(HK)\right]\right]^2+\left[b_{\mathrm{Cu}}+2b_{\mathrm{Cl}}\cos\left[-\frac{z_0}{c_0}\pi L+\phi(HK)\right]\right]^2\right\}[1+(-1)^{H+L}]\,. \quad (2)$$

Similarly for the graphite layer, the unit-cell scattering function can be described by

$$S_{\mathrm{G}(HKL)}=4b_c^2\cos^2\left[\frac{2\pi}{3}(H-K)\right]\times\left[2+\cos\left[\frac{2\pi}{3}(H-K)+\pi L\right]+\cos\left[\frac{2\pi}{3}(H-K)-\pi L\right]\right]. \quad (3)$$

This model has two free parameters, z_0 and p. From fitting intensities of the $(00L)$ x-ray scan, we find $z_0=1.31\pm0.03$ Å, which is slightly smaller than the value for pristine $CuCl_2$. The fits are insensitive to p, and we have therefore fixed p at 0.75, its value in the pristine compound. This value is also required by our observation from ESR that the local crystal field at the Cu^{2+} sites is tetragonal (see Sec. IV C).

While this model accounts for the peak positions and intensities qualitatively, it overestimates intensities at high L and predicts sharp peaks rather than the broad ones observed. This situation holds for all values of z_0 and p considered. The discrepancy can be explained by the large mosaic spread and the presence of stacking faults.

B. Magnetic susceptibility

Figure 8(a) shows the temperature dependence of the dc magnetic susceptibility of stage-1, stage-2, and stage-3 $CuCl_2$ GIC's (sample nos. 2, 3, and 4, respectively). Between 150 and 300 K these data are well described by the sum of a Curie-Weiss term and a temperature-independent term:

$$\chi=\frac{C_H}{T-\Theta_H}+\chi_H^0\,. \quad (4)$$

Figure 8(b) shows the reciprocal susceptibility $(\chi-\chi_H^0)^{-1}$ as a function of temperature for stage-2 $CuCl_2$ GIC. The data agree well with a straight line predicted from the

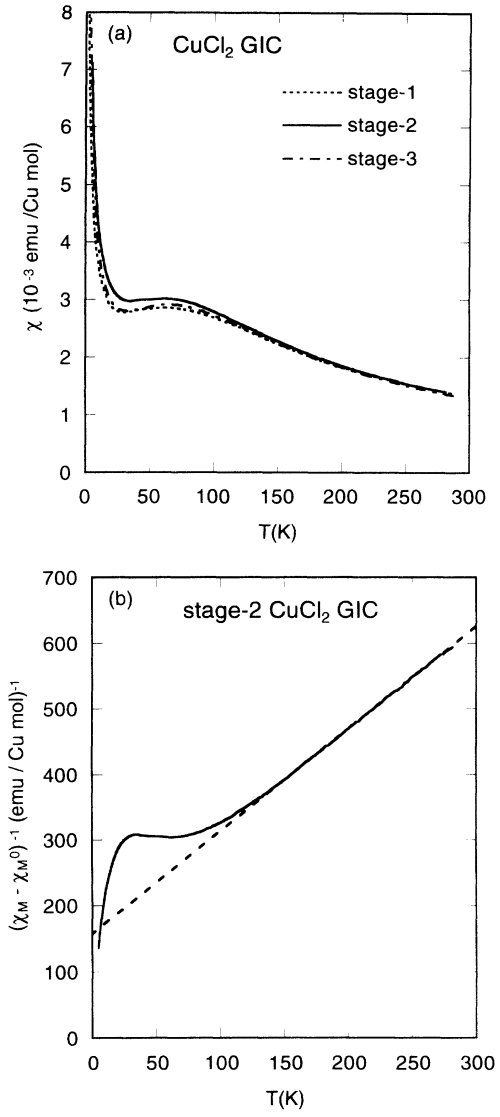

FIG. 8. (a) Temperature variation of dc magnetic susceptibility perpendicular to the c axis for stage-1, stage-2, and stage-3 $CuCl_2$ GIC's. (b) Temperature variation of reciprocal susceptibility $(\chi-\chi_0^H)^{-1}$ for stage-2 $CuCl_2$ GIC where $\chi_0^H=-0.280\times10^{-3}$ emu/Cu mol. The straight line denotes the Curie-Weiss law with $\Theta_H=-100.9$ K and $C_H=0.641$ emu K/Cu mol.

Curie-Weiss law at high temperatures, but deviate from this below 150 K due to the growth of magnetic short-range order.

Least-squares fits to Eq. (4) for $150\le T\le300$ K yield parameters that are listed in Table III. The Curie-Weiss constant C_H, the Curie-Weiss temperature Θ_H, and the temperature-independent susceptibility χ_H^0 are almost independent of stage number. However, the slight stage-dependence is reproduced with other samples to within about 1%. It is particularly interesting that stage-2 parameters do not lie between the parameters for stage-1 and stage-3 samples. Such behavior is not understood, although it has been seen also for $CoCl_2$ GIC's.[28]

From the Curie-Weiss constant we determine the effective magnetic moment, $P_{\rm eff}=[(3k_B/N_A\mu_B^2)C_H]^{1/2}$, of the Cu^{2+} spins as $2.33\mu_B$, $2.26\mu_B$, and $2.39\mu_B$ for stage-1, stage-2, and stage-3 $CuCl_2$ GIC's, respectively. These values of $P_{\rm eff}$ are larger than that expected for free Cu^{2+} $(1.73\mu_G)$.[29] The negative sign of Θ_H indicates that the exchange interactions between Cu^{2+} spins are antiferromagnetic. According to molecular field theory, the Curie-Weiss temperature of these systems can be described by[29]

$$\Theta_H=\tfrac{2}{3}zS(S+1)\langle J\rangle=3\langle J\rangle\ , \tag{5}$$

where $S=\frac{1}{2}$, $z=6$, and $\langle J\rangle$ is the average exchange interaction. From the observed Θ_H values we estimate $\langle J\rangle=-39\pm1$ K for stage-1, -34 ± 1 K for stage-2, and -39 ± 1 K for stage-3 $CuCl_2$ GIC.

The temperature-independent term in Eq. (4) is the sum of several contributions: the core diamagnetism χ_0, the Pauli susceptibility χ_p, and the intra- and interband contributions due to orbital motion of electrons in the graphite layers.[30] Estimates of the first contribution[31] yield values of χ_H^0 that are roughly one-third of the fitted values. The other terms can be estimated from the susceptibility of graphite,[30] whose room-temperature in-plane susceptibility is -0.005×10^{-3} emu/mol of carbon. Adding this directly to the core contribution again estimates χ_H^0 much smaller in magnitude than observed. However, the out-of-plane diamagnetic susceptibility of graphite is much larger (-0.253×10^{-3} emu/mol) than that in the *a-b* plane.[30] Adding contributions from misaligned crystallites brings the expected diamagnetic susceptibility into closer agreement with the fitted values

TABLE III. Curie-Weiss temperature Θ_H, Curie-Weiss constant C_H, and temperature-independent susceptibility χ_0^H from fits to high-temperature (150–300 K) susceptibility data; temperature $T_{\rm max}$ and susceptibility $\chi_{\rm max}$ at which dc susceptibility has a maximum in the paramagnetic region. $\langle J\rangle$ is the average exchange interaction, determined from Θ_H by Eq. (5). Data are shown for stage-1, stage-2, and stage-3 $CuCl_2$ GIC's, and for pristine $CuCl_2$ for comparison (Refs. 18 and 20).

Sample number	Stage number	Θ_H (K)	C_H (emu K/mol)	χ_0^H (10^{-3} emu/mol)	$T_{\rm max}$ (K)	$\chi_{\rm max}$ (10^{-3}emu/mol)	$\langle J\rangle$ (K)
2	1	−118	0.677	−0.299	65	2.858	−39
3	2	−101	0.641	−0.280	62	3.014	−34
4	3	−117	0.713	−0.434	65	2.914	−39
Pristine	$CuCl_2$	−109	0.536		70	2.43	

of χ_H^0, given in Table III.

As shown in Fig. 8(a) the susceptibility of $CuCl_2$ GIC's exhibits a broad peak of magnitude χ_{max} at the temperature T_{max}. The values of χ_{max} and T_{max} are listed in Table III; they, too, are almost independent of stage number and are close to those of pristine $CuCl_2$. Apart from this broad peak, there is no anomaly in the dc magnetic susceptibility above 1.5 K. This result is consistent with the expected behavior of both 1D and 2D Heisenberg antiferromagnets, both of which exhibit broad peaks in susceptibility and show no magnetic long-range order at any temperature.[24]

We first consider the 2D case. To our knowledge there is no theoretical prediction for the susceptibility of a 2D Heisenberg antiferromagnet on a *regular* triangular lattice, let alone an *isosceles* lattice. For discussion here we will assume that the susceptibility coincides with that of an antiferromagnet on a square lattice with near-neighbor exchange constant J. The latter system is predicted to show a maximum susceptibility of magnitude

$$\chi_{max}=0.0469\left[\frac{N_A g^2\mu_B^2}{k_B|J|}\right]=\frac{0.0176}{|J|}g^2(\text{emu/mol}) \quad (6)$$

at the temperature $T_{max}=2.53\ S(S+1)|J|=1.898|J|$.[32] Using these expressions with the stage-2 values for χ_{max} and T_{max}, we predict an effective exchange interaction of -30 ± 3 K. This agrees fairly well with the observed $\langle J\rangle$ value of -34 K for the stage-2 sample.

On the other hand, for a 1D Heisenberg $S=\frac{1}{2}$ antiferromagnet with near-neighbor exchange constants J, the susceptibility is predicted to show a broad peak of magnitude

$$\chi_{max}=0.073\,46\left[\frac{N_A g^2\mu_B^2}{k_B|J|}\right]=\frac{0.0276}{|J|}g^2(\text{emu/mol}) , \quad (7)$$

located at the temperature $T_{max}=1.282|J|$.[33] Using the experimentally determined stage-2 values for χ_{max} and T_{max} with these 1D predictions leads to an effective interaction $J=-45\pm3$ K. This is considerably higher than the value of $\langle J\rangle$ we obtain from high-temperature susceptibility. Therefore, the 1D model is not as satisfactory a description as the 2D Heisenberg model is. We point out that our interpretation of the susceptibility in terms of 2D magnetic behavior differs from the analysis of Rancourt *et al.*,[13] who have attempted to show that $CuCl_2$ GIC's approximate finite linear chain magnets.

The dc magnetic susceptibility of $CuCl_2$ GIC's shows a Curie-Weiss-like increase below 20 K that is not observed in the pristine compound. We ascribe this behavior to paramagnetic impurities present in the system. A least-squares fit of the susceptibility data in the temperature range $4\le T\le 18$ K to the Curie-Weiss law

$$\chi_L=\frac{C_L}{T-\Theta_L}+\chi_0^L , \quad (8)$$

yields the values of C_L, Θ_L, and χ_0^L listed in Table IV. The value of Θ_L is positive but very close to zero, which indicates that Cu^{2+} spins contributing to this susceptibility are essentially noninteracting. The fraction f of Cu^{2+} spins that are noninteracting is given by $f=C_L/C_H$, where C_H is described in Eq. (4). These fractions are listed in Table IV for all three stages and are a few percent. The temperature-independent constant χ_0^L represents a sum of several other terms that do not vary appreciably over the narrow temperature range of the fit.

The paramagnetic behavior may arise from inhomogeneities across the intercalate islands.[11] The fraction of spins residing at the perimeter of a circular island is roughly $2\sqrt{3}\langle a\rangle/\xi$, where $\langle a\rangle$ is the average distance between spins and ξ is the island diameter. Taking this as the noninteracting fraction f, we estimate the island sizes as $\xi=360-670$ Å for the $CuCl_2$ GIC's. Although there have been no direct measurements of the island size in $CuCl_2$ GIC's, these values are on the same order as those observed in $CoCl_2$ GIC, $NiCl_2$ GIC, and $MnCl_2$ GIC.[5,6] It is therefore plausible, at least, that spins near the periphery of intercalate islands behave paramagnetically.

C. Electron spin resonance

The energy-level diagram of the Cu^{2+} ion in an octahedral crystal field has been widely studied in many of its compounds, such as copper benzoate[34] and $CuCl_2$-$2H_2O$.[35] The ground state has an (x^2-y^2)-type wave function (Ψ_4) with energy E_4. The first excited state has a z^2-type wave function (Ψ_5) with energy E_5. The second excited state has an xy type wave function (Ψ_3) with energy E_3. The third excited states are doubly degenerate and have yz-type wave functions (Ψ_2) and zx-type wave functions (Ψ_1) with energy $E_{1,2}$.

The g values along the z axis and the x axis are predict-

TABLE IV. Curie-Weiss temperature Θ_L, Curie-Weiss constant C_L, and the temperature-independent susceptibility χ_0^L, from fits to low-temperature (4–18 K) susceptibility data. The ratio of low- to high-temperature Curie-Weiss constants is given as $f=C_L/C_H$ for stage-1, stage-2, and stage-3 $CuCl_2$ GIC's.

Sample number	Stage number	Θ_L (K)	C_L (emu K/mol)	χ_0^L (10^{-3} emu/mol)	f
2	1	0.96±0.06	0.012	2.33	0.017
3	2	0.69±0.07	0.020	2.16	0.032
4	3	1.43±0.09	0.015	2.18	0.021

ed to be[34]

$$g_z = g_e\left[1-\frac{4\lambda}{E_3-E_4}\right],$$
$$g_x = g_e\left[1-\frac{\lambda}{E_{1,2}-E_4}\right], \tag{9}$$

respectively, where $g_e=2.0023$ and λ is the spin-orbit coupling constant ($\lambda\approx -850$ cm^{-1}) for the Cu^{2+} ion. Here we have assumed no g anisotropy in the x-y plane. The angular dependence of the g factor of the Cu^{2+} ion of $CuCl_2$ GIC is described by the classical formula[35]

$$g^2(\theta,\phi_0)=g_z^2\sin^2\theta\cos^2\phi_0+g_x^2\sin^2\theta\sin^2\phi_0+g_x^2\cos^2\theta\ , \tag{10}$$

for the rotation of magnetic field **H** in the a'-b' (intercalate) plane. Here $\phi_0=31°$ is the angle between the z axis and the a' axis and θ is the angle between **H** and the b' axis [see Fig. 1(d)]. Since $g_z>g_x$, g takes a minimum at $\theta=0°$ (along the b' axis) and a maximum at $\theta=90°$ (along the a' axis):

$$g_{\max}=[g_z^2\cos^2\phi_0+g_x^2\sin^2\phi_0]^{1/2}$$
and
$$g_{\min}=g_x\ . \tag{11}$$

We have studied the ESR of stage-1, stage-2, and stage-3 $CuCl_2$ GIC's (sample nos. 2, 3, and 4) with microwaves of frequency $\nu=22.83$ GHz. The ESR spectrum has a Lorentzian line shape. Figure 9(a) shows the angular dependence of g^2 for stage-2 $CuCl_2$ GIC (sample no. 3). There are three sinusoidal curves of period 180°, giving direct evidence that the $CuCl_2$ intercalate layer consists of domains I, II, and III. In agreement with Eq. (11), each curve has a minimum for **H**$\|$**b'** and a maximum for **H**$\|$**a'** of each domain. This angular dependence is similar for stage-1 and stage-3 $CuCl_2$ GIC's. Least-squares fits to Eq. (11) yield values of $g_x=2.08\pm0.01$ and $g_z=2.30\pm0.01$, independent of stage number. From these the g value along the c axis is estimated as

$$g_c=[g_z^2\sin^2\phi_0+g_x^2\cos^2\phi_0]^{1/2}=2.13\ .$$

The ratios of spin-orbit coupling to Cu^{2+} energy level splittings are given from Eq. (9) as $\lambda/(E_3-E_4)=-0.037$ and $\lambda/(E_{1,2}-E_4)=-0.039$.

The difference between g_x and g_z indicates that the spin Hamiltonian in $CuCl_2$ GIC's is anisotropic. Since $S=\frac{1}{2}$, there can be no single-ion anisotropy term,[36] and the source of the anisotropy must be exchange. In order to estimate the size of the exchange anisotropy (and therefore its effect on the spin symmetry), we have measured the peak-to-peak linewidth ΔH_{pp} of the ESR absorption line. Figure 9(b) shows the angular dependence of ΔH_{pp} at 4.2 K in the a'-b' plane for domain I of stage-2 $CuCl_2$ GIC (sample no. 3). The linewidth is found to fit well to the solid curve empirically expressed by $\Delta H_{pp}=146.8-55.9\cos(2\theta)$ (Oe).

The angular dependence of ΔH_{pp} is explained by the

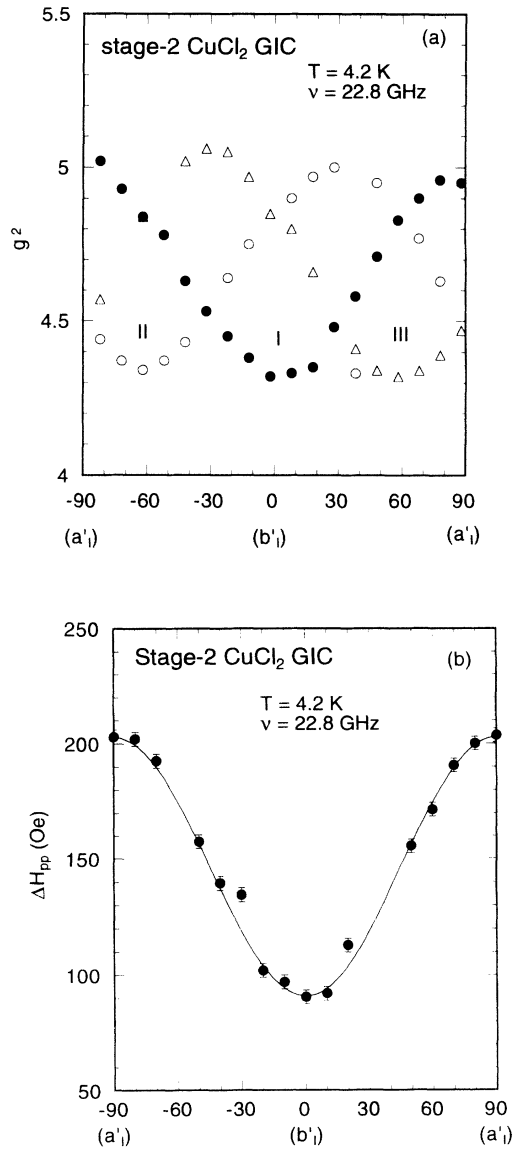

FIG. 9. (a) Angular dependence of g^2 in the a'-b' plane of stage-2 $CuCl_2$ GIC, consisting of three curves arising from domains I, II, and III. Here θ is an angle between an external magnetic field **H** and the b' axis of domain I. (b) Angular dependence of the linewidth ΔH in the a'-b' plane of stage-2 $CuCl_2$ GIC. Only a curve from domain I is shown for simplicity. $T=4.2$ K, $\nu=22.8$ GHz.

contribution of anisotropic exchange interaction and dipolar interaction to the linewidth as follows. The ESR linewidth of the $CuCl_2$ GIC at high temperatures may be dominated by long-wavelength modes ($\mathbf{q}=0$) of the spin correlation function. As the temperature goes down to 4.2 K, the $\mathbf{q}=0$ contribution is no longer of importance. At low temperatures the short time decay of the spin-correlation function may become dominant. Then the linewidth is considered to be proportional to the total second moment consisting of secular and nonsecular parts. Here we use a form of the total second moment

similar to that first derived by Date *et al.*[34] They have discussed the effect of dipolar interaction and anisotropic exchange interaction on the linewidth of the linear chain antiferromagnet copper benzoate in terms of a theory of Kubo and Tomita.[37] According to Date *et al.*,[34] the linewidth in $CuCl_2$ GIC may be described as

$$\Delta H \approx \zeta[A^2(\cos^2\gamma+1)+4B^2(\cos^2\theta+1) -2AB(3\cos^2\gamma-1)(3\cos^2\theta-1)] , \quad (12)$$

in the a'-b' plane as shown in Fig. 1(d), where ζ is a constant, γ is the angle between the z axis (the tetragonal axis) and the external magnetic field $\mathbf{H}$, θ is the angle between the b' axis and the field $\mathbf{H}$. There is a simple relationship between γ and θ; $\cos^2\gamma=\cos^2\phi_0\sin^2\theta$. The anisotropic exchange interaction has the form

$$H_{\rm an}=\sum_{\langle i,j\rangle}(S_i^x\cdot A_{ij}^{xx}\cdot S_j^x+S_i^y\cdot A_{ij}^{yy}\cdot S_j^y+S_i^z\cdot A_{ij}^{zz}\cdot S_j^z) , \quad (13)$$

where $A=A_{ij}^{zz}=-2A_{ij}^{xx}=-2A_{ij}^{yy}$ because of tetragonal symmetry. The constant A is on the order of $A\approx(\Delta g/\langle g\rangle)^2\langle J\rangle$, where Δg is the anisotropy of the g value and $\langle g\rangle$ is the average of the g value. The constant B is a dipole-dipole interaction given by $B\approx\langle g\rangle^2\mu_B^2/|\mathbf{r}|^3$, where $|\mathbf{r}|$ is the nearest-neighbor distance between Cu atoms. Note that ΔH reduces to a conventional form of $\Delta H\approx 4\zeta B^2(1+\cos^2\theta)$ for the case of $A=0$. The values of A and B are estimated as $A=-0.38$ K and $B=0.08$ K for stage-2 $CuCl_2$ GIC, where $\langle J\rangle=-33.6$ K, $g_x=2.08$, $g_z=2.31$, $\langle g\rangle=2.16$, and $|\mathbf{r}|=a$. Since $|\langle J\rangle|\gg|A|$, as was discussed before, $CuCl_2$ GIC's is considered to be a 2D Heisenberg antiferromagnet. The value of B is much smaller than that of $|\mathbf{A}|$. When $\mathbf{B}=0$ is assumed, the linewidth ΔH is simply described by

$$\Delta H\approx\zeta A^2(\cos^2\gamma+1) =\zeta A^2[(1+\tfrac{1}{2}\cos^2\phi_0)-\tfrac{1}{2}\cos^2\phi_0\cos 2\theta] . \quad (14)$$

For the case of $\zeta A^2\approx 117$ Oe, the linewidth ΔH has a minimum value ($=117$ Oe) at $\theta=0°$ and a maximum value ($=203$ Oe) at $\theta=90°$, in good agreement with observations for stage-2 $CuCl_2$ GIC. The result shows that the anisotropic exchange interaction contributes dominantly to the linewidth of this compound.

D. Search for a magnetic phase transition

There have been several prior suggestions of a phase transition in $CuCl_2$ GIC's and predictions of phase transitions in the systems they are expected to approximate. In a study of stage-1 $CuCl_2$ GIC, Nishihara *et al.*[11] reported that the difference between the measured dc magnetic susceptibility χ and the low-temperature Curie-Weiss term χ_L, $\Delta\chi=\chi-\chi_L$, exhibits a small peak at $T_0=14$ K, in addition to the broad peak at $T_{\rm max}$. The characteristic temperature T_0 is below the Néel temperature in pristine $CuCl_2$ (23.9 K),[18–23] and it was speculated to be due to a magnetic phase transition.[11] No similar anomaly was found for stage-2 or stage-3 samples. Rancourt, Meschi, and Flandrois[13] also reported data for stage-2 $CuCl_2$ GIC's that showed small peaks in susceptibility around 8.5 K after the low-temperature susceptibility is subtracted. They explained them, however, as an artifact of their data reduction scheme. We have applied the method of Nishiara *et al.*[11] to our data. Contrary to their results and those of Rancourt, Meschi, and Flandrois,[13] we find no peak in $\Delta\chi$ for any stage $CuCl_2$ GIC.

In the Introduction we suggested that $CuCl_2$ GIC's may be a model system for studying the critical behavior of the 2D Heisenberg AFT system. The phase transition of this model is thought to be mediated by vortices of local chirality vectors.[4] Pairing of these vortices occurs below the Kawamura-Miyashita temperature $T_{\rm KM}=0.66|\langle J\rangle|S^2$ and is accompanied by a broad peak in the heat capacity, but no anomaly in the susceptibility,[4] consistent with our findings for $CuCl_2$ GIC's. If these predictions hold for $CuCl_2$ GIC's, then using $\langle J\rangle=-34$ K we can estimate $T_{\rm KM}=5.5$ K. According to the theory, the spin-correlation function decays exponentially with distance both above and below $T_{\rm KM}$.[4]

In order to examine whether a magnetic phase transition occurs in $CuCl_2$ GIC's, we have performed neutron-diffraction experiments on stage-1 $CuCl_2$ GIC down to 0.5 K. We have taken data along (00L), (*HK*0), Cu(10L), and Cu(01L), and for in-plane scans at $L=0.336$ and 0.672 Å^{-1} (representing, respectively, $L=\frac{1}{2}$ and 1 in reciprocal-lattice units indexed to stage 1). The scan directions are shown in Fig. 7. The magnetic contribution to the total scattering was measured by subtracting from the data analogous scans performed at high temperatures, where the magnetic scattering is featureless. Figure 10 shows a typical difference scan, taken along the (*HK*0) direction. No peaks are seen in this scan or in any other scan we performed, suggesting that there is no magnetic phase transition above 0.5 K.

There are several other reasons why we might not observe magnetic scattering, however. The first possibility is that we looked in the wrong place. This is unlikely for

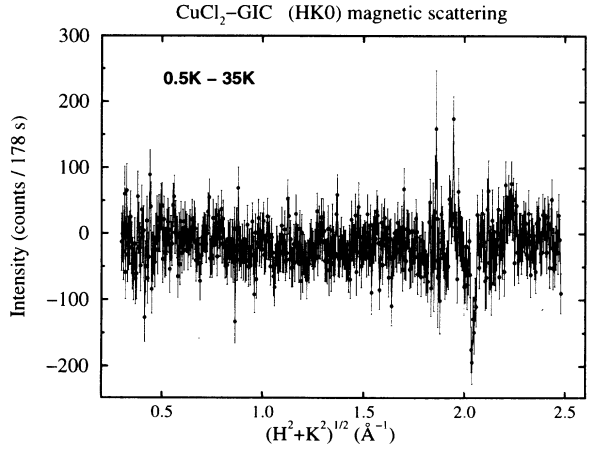

FIG. 10. Representative difference curve showing no magnetic scattering at 0.5 K. This curve represents the difference between (*HK*0) scans at 0.5 and 35 K, above any ordering temperature. Data were collected on BT2. The sharp feature at 1.9 Å^{-1} is an artifact of thermal expansion. Similar data were obtained for (*HK*1) scans.

the following reasons. Our sample is a 2D powder, so any magnetic scattering must have some intersection with the scattering plane. Near (and above) any phase transition, the scattering is likely to be either 2D (appearing as rods) or 1D (appearing as sheets); either of these distributions would be seen in an (*HK*0) scan. If the scattering is 3D (Bragg points), then it is unlikely that the structure factor would cause the intensity to vanish *everywhere* along the Cu(10*L*) and Cu(10*L*) rods.

A second possible reason we see no magnetic scattering is that it is too weak to be seen over the background. We estimate here how strong the magnetic scattering might be expected to be. The nuclear scattering cross section for a system of scatterers at positions $\mathbf{r}_i$ is given by[27]

$$\left[\frac{d\sigma}{d\Omega}\right]_N(\mathbf{Q})=\sum_{i,j} b_i b_j \exp[-i\mathbf{Q}\cdot(\mathbf{r}_i-\mathbf{r}_j)] , \tag{15}$$

while the magnetic cross section is

$$\left[\frac{d\sigma}{d\Omega}\right]_M(\mathbf{Q})=|\tfrac{1}{2}r_0\gamma g|^2 \sum_{i,j} |f(Q)|^2 \mathbf{S}_i^{\perp}\cdot\mathbf{S}_j^{\perp}\exp[-i\mathbf{Q}\cdot(\mathbf{r}_1-\mathbf{r}_j)] , \tag{16}$$

where r_0 is the classical electron radius, γ is the neutron gyromagnetic ratio, $f(Q)$ is the magnetic form factor, and $\mathbf{S}_i^{\perp}$ is the component of the spin vector at the site $\mathbf{r}_i$ perpendicular to the scattering plane. If the magnetic correlations are comparable to structural ones, and if we assume maximum constructive interference of scattered waves for both the magnetic and the nuclear cross section, then the ratio of magnetic to nuclear intensities for $CuCl_2$ GIC's is roughly

$$\frac{|r_0\gamma g/2|^2|f(Q)|^2 S(S+1)/2}{(b_{\mathrm{Cu}}+2b_{\mathrm{Cl}})^2}\approx 0.5-1\ \% . \tag{17}$$

The condition of maximum constructive interference is nearly met for the Cu(110) reflection, which by Fig. 5 gives 5400 counts in 77 sec. 1% of this value would predict a magnetic scattering peak in Fig. 10 with 125 counts, which is well above the background. In fact, the argument is stronger than this: Because of the powder nature of the sample, intensities drop as $1/(H^2+K^2)^{1/2}$. This indicates that magnetic scattering in Fig. 5 at, say, 1.1 Å^{-1}, would appear three times as intense as the 125 counts predicted above.

If the magnetic correlations are of lower dimensionality than the structural correlations, they will also be weaker and more diffuse in reciprocal space. However, this fact does not affect the argument as much as one might at first think. The nuclear peaks in Fig. 5 are already broadened substantially by stacking faults and mosaicity, which spreads the intensity out in rods along L instead of concentrating it at Bragg spots. A rough measure of this effect can be gauged by comparing the peak intensity to the L-averaged intensity in Figs. 6(a) and 6(b). If all the intensity were to be uniformly distributed in L, there would be about 3000 counts in 2 min along the Cu(01*L*) or Cu(10*L*). 1% of this would predict 90 counts at 1 Å^{-1} on Fig. 10, even for 2D magnetic rods. This is above the background level, as well.

Scattering due to 1D magnetic correlations would be still more diffuse, roughly comparable to the noise level in the difference scans we have taken. Very short in-plane correlations would broaden the reflections, thereby reducing their intensity. We estimate that if these correlations were shorter than about 15 Å (for 3D correlations) or 40 Å (for 2D correlations), then the magnetic intensities would be too small to see in our data. It is therefore consistent with our data for the Cu^{2+} spins to exhibit either 1D correlations or weak 2D or 3D correlations at low temperatures, as long as they are sufficiently short ranged.

All the predictions above concern *classical* spins. Yet quantum models are certainly more appropriate to describe the $S=\frac{1}{2}$ Cu^{2+} spins in $CuCl_2$ GIC's. Quantum effects are thought to exert a profound influence on the critical behavior of low-dimensional magnets (see, for example, the so-called Haldane conjecture for linear chain antiferromagnets[38]). While no calculations on the isosceles lattice have been carried out for quantum antiferromagnets, the consensus is that the $S=\frac{1}{2}$ antiferromagnet on a regular triangular lattice shows no magnetic long-range order, even at $T=0$ K.[39] Our results on the distorted lattice for $CuCl_2$ GIC's are consistent with this theoretical understanding.

V. CONCLUSION

We have investigated the structural and magnetic properties of stage-1, stage-2, and stage-3 $CuCl_2$ GIC's. In all compounds the $CuCl_2$ intercalate layer forms an isosceles triangular lattice with lattice constants $a=3.28$ Å and $b=3.77$ Å, and with an angle between them of 115.8°. The intercalate plane is nearly the same as the a'-b' plane in monoclinic $CuCl_2$. The $CuCl_2$ layer is incommensurate with the graphite layer, but the a_G axis of the graphite layer coincides with the intercalate a axis.

High-temperature susceptibility shows that the average exchange interaction between Cu^{2+} spins $\langle J\rangle$ is -39 K for stage-1, -34 K for stage-2, and -39 K for stage-3 $CuCl_2$ GIC. Position and magnitude of a broad susceptibility maximum are more consistent with a 2D Heisenberg model than with the 1D model. The anisotropy of the ESR data can be explained in terms of a local tetragonal symmetry of Cu^{2+} spins, such that the tetragonal axis (the z axis) is canted away from the c axis by 59°. The values of g_x and g_z are determined as $g_x=2.08\pm0.01$ and $g_z=2.30\pm0.01$, independent of stage number, and the anisotropic exchange interaction A is much smaller than

$\langle J \rangle$. Thus, the $CuCl_2$ GIC's behave like 2D Heisenberg antiferromagnets on an isosceles triangular lattice. No sign of magnetic scattering was observed in neutron-diffraction data above 0.5 K, strongly suggesting that the magnetic correlation lengths are less than 40 Å at this temperature.

ACKNOWLEDGMENTS

We would like to thank H. Kawamura for valuable discussions on the in-plane spin structure. H. Suematsu for providing us with high-quality single crystals of kish graphite, and F. Khemai and W. Brinkman for their help on x-ray scattering and dc magnetic susceptibility measurements. The preliminary neutron-diffraction experiment was carried out when one of us (M.S.) was at the University of Illinois at Urbana-Champaign. We would like to thank H. Zabel for providing us with the opportunity to use the neutron scattering facility at Oak Ridge National Laboratory. We are also grateful to H. Yasuoka for the use of the ESR facility, and M. Ichihara and K. Suzuki for doing electron diffraction, at the Institute for Solid State Physics, University of Tokyo. The work at SUNY-Binghamton was supported by NSF DMR-8902351 and DMR-9201656.

[1]G. M. Wannier, Phys. Rev. **79**, 357 (1950).
[2]S. Miyashita and H. Shiba, J. Phys. Soc. Jpn. **53**, 1145 (1984).
[3]D. H. Lee, J. D. Joannopoulos, J. W. Negele, and D. P. Landau, Phys. Rev. Lett. **52**, 433 (1984).
[4]H. Kawamura and S. Miyashita, J. Phys. Soc. Jpn. **53**, 4138 (1984).
[5]M. Suzuki, Crit. Rev. Solid State Mater. Sci. **16**, 237 (1990).
[6]G. Dresselhaus, J. T. Nicholls, and M. S. Dresselhaus, in *Graphite Intercalation Compounds II,* edited by H. Zabel and S. A. Solin (Springer-Verlag, New York, 1992), p. 247.
[7]Y. Kimishima, A. Furukawa, M. Suzuki, and H. Nagano, J. Phys. C **19**, L43 (1986).
[8]M. Suzuki, D. G. Wiesler, P. C. Chow, and H. Zabel, J. Magn. Magn. Mater. **54-57**, 1275 (1986).
[9]M. Matsuura, Y. Karaki, T. Yonezawa, and M. Suzuki, Jpn. J. Appl. Phys. Suppl. **26-3**, 773 (1987).
[10]M. Suzuki, in *Extended Abstracts of the Symposium on Graphite Intercalation Compounds: Science and Applications,* edited by M. Endo, M. S. Dresselhaus, and G. Dresselhaus (Materials Research Society, Pittsburgh, 1988), p. 65.
[11]H. Nishihara, I. Oguro, M. Suzuki, K. Koga, and H. Yasuoka, Synth. Met. **12**, 473 (1985).
[12]K. Koga, M. Suzuki, and H. Yasuoka, Synth. Met. **12**, 467 (1985).
[13]D. G. Rancourt, C. Meschi, and S. Flandrois, Phys. Rev. B **33**, 347 (1986).
[14]D. G. Wiesler, Ph. D. thesis, University of Illinois at Urbana-Champaign, 1989.
[15]C. Hauw, J. Gaultier, S. Flandrois, O. Gonzalez, O. Dorignac, and R. Jagut, Synth. Met. **7**, 313 (1983).
[16]J. S. Speck, J. T. Nicholls, B. J. Wuensch, J. M. Delgado, and M. S. Dresselhaus, Philos. Mag. B **64**, 181 (1991).
[17]A. F. Wells, J. Chem. Soc. 1670 (1947).
[18]C. Starr, F. Bitter, and A. R. Kaufmann, Phys. Rev. **58**, 977 (1940).
[19]J. W. Stout and R. C. Chisholm, J. Chem. Phys. **36**, 979 (1962).
[20]D. Billerey, C. Terrier, R. Mainard, M. Perrin, and J. Hubsch, Phys. Lett. **68A**, 275 (1978).
[21]D. Billerey and C. Terrier, Phys. Lett. **68A**, 278 (1978).
[22]D. Billerey and C. Terrier, Phys. Lett. **77A**, 196 (1980).
[23]D. Billerey, C. Terrier, R. Mainard, N. Ciret, and A. J. Pointon, J. Magn. Magn. Mater. **30**, 55 (1982).
[24]L. J. de Jongh and A. R. Miedema, Adv. Phys. **23**, 1 (1974).
[25]S. Hendricks and E. Teller, J. Chem. Phys. **10**, 147 (1942).
[26]I. S. Suzuki and M. Suzuki, J. Phys.: Condens. Matter **3**, 8825 (1991).
[27]G. E. Bacon, *Neutron Diffraction* (Clarendon, Oxford, 1975); S. W. Lovesey, *Theory of Neutron Scattering from Condensed Matter* (Oxford University Press, Oxford, 1984).
[28]D. G. Wiesler, M. Suzuki, P. C. Chow, and H. Zabel, Phys. Rev. B **34**, 7951 (1986).
[29]C. Kittel, *Introduction to Solid State Physics* (Wiley, New York, 1986), p. 406.
[30]F. J. DiSalvo, S. A. Safran, J. V. Wasczak, and J. E. Fischer, Phys. Rev. B **20**, 4883 (1979).
[31]L. N. Mulay, *Magnetic Susceptibility* (Interscience, New York, 1966).
[32]R. Navarro, in *Magnetic Properties of Layered Transition Metal Compounds,* edited by L. J. de Jongh (Kluwer Academic, Boston, 1990), p. 105, see also its references.
[33]J. C. Bonner and M. E. Fisher, Phys. Rev. **135**, A640 (1964).
[34]M. Date, H. Yamazaki, M. Motokawa, and S. Tazawa, Suppl. Prog. Theor. Phys. **46**, 194 (1970).
[35]Y. Servant, J. C. Bissey, and M. Maini, Phyisca B **106**, 343 (1981).
[36]See, for example, K. W. H. Stevens, in *Magnetism,* edited by G. T. Rado and H. Suhl (Academic, New York, 1963), Vol. I, p. 1.
[37]R. Kubo and K. Tomita, J. Phys. Soc. Jpn. **9**, 80 (1954).
[38]F. D. M. Haldane, Phys. Rev. Lett. **50**, 1153 (1983).
[39]N. D. Mermin and H. Wagner, Phys. Rev. Lett. **17**, 1133 (1966); T. Oguchi, H. Nishimori, and Y. Taguchi, J. Phys. Soc. Jpn. **55**, 323 (1986); S. Fujiki, Can. J. Phys. **65**, 489 (1987); D. D. Betts and S. Miyashita, *ibid.* **68**, 1410 (1990).